

## Retrieving optically thick ice cloud microphysical properties by using airborne dual-wavelength radar measurements

Zhien Wang,<sup>1</sup> Gerald M. Heymsfield,<sup>2</sup> Lihua Li,<sup>3,4</sup> and Andrew J. Heymsfield<sup>5</sup>

Received 12 March 2005; revised 20 May 2005; accepted 22 June 2005; published 4 October 2005.

[1] An algorithm to retrieve optically thick ice cloud microphysical property profiles is developed by using the GSFC 9.6 GHz ER-2 Doppler Radar (EDOP) and the 94 GHz Cloud Radar System (CRS) measurements aboard the high-altitude ER-2 aircraft. In situ size distribution and total water content data from the CRYSTAL-FACE field campaign are used for the algorithm development. To reduce uncertainty in calculated radar reflectivity factors ( $Z_e$ ) at these wavelengths, coincident radar measurements and size distribution data are used to guide the selection of mass-length relationships and to deal with the density and nonspherical effects of ice crystals on the  $Z_e$  calculations. The algorithm is able to retrieve microphysical property profiles of optically thick ice clouds, such as deep convective and anvil clouds, which are very challenging for single-wavelength radar and lidar. Examples of retrieved microphysical properties for deep convective clouds are presented, which show that EDOP and CRS measurements provide rich information to study cloud structure and evolution. Good agreement between IWPs derived from an independent submillimeter-wave radiometer, CoSSIR, and dual-wavelength radar measurements indicates accuracy of the IWC retrieved from the dual-wavelength radar algorithm.

**Citation:** Wang, Z., G. M. Heymsfield, L. Li, and A. J. Heymsfield (2005), Retrieving optically thick ice cloud microphysical properties by using airborne dual-wavelength radar measurements, *J. Geophys. Res.*, 110, D19201, doi:10.1029/2005JD005969.

### 1. Introduction

[2] Ice clouds play a significant role in the atmospheric water and energy cycles [Wielicki *et al.*, 1995]. High cold cirrus clouds affect the Earth's energy balance through both greenhouse and albedo effects. Because they are normally optically thin, we can observe cirrus with many different methods [Lynch *et al.*, 2002]. There have been several research programs aimed at better understanding cirrus, most recently the Cirrus Regional Study of Tropical Anvils and Cirrus Layers—Florida Area Cirrus Experiment (CRYSTAL-FACE) field campaign (<http://cloud1.arc.nasa.gov/crystalface/>). However, the global net impact of cirrus is still unknown [Liou, 1986; Lynch *et al.*, 2002]. Deep convective and nimbostratus clouds are the main players in the atmospheric water cycle by redistributing water globally. The upper parts of these clouds are mainly ice and much of the condensate that does not reach the ground exits into the anvils of these clouds that can form extensive cirrus layers. These cirrus layers are important for the

radiation budget. To improve our weather and climate forecast capability, accurate representations of ice regions are needed in models. This requires the advanced knowledge of the vertical distributions of ice cloud microphysical properties and their spatial and temporal variations in different types of ice clouds.

[3] Although there are substantial advances in our remote sensing capability, it is still difficult to obtain microphysical property profiles in optically thick ice clouds, such as anvil clouds and upper parts of deep convective clouds. Algorithms based on lidar and radar measurements provide ice cloud microphysical property profiles [Donovan and Van Lammeren, 2001; Wang and Sassen, 2002]. However, these algorithms can only be applied to ice clouds where the integrated optical depth reaches  $\sim 3$  which lidar is able to penetrate. Algorithms using passive IR and solar radiance measurements can retrieve cloud properties with an optical depth larger than 3, but only for layer integrated properties. Algorithms using microwave measurements are best suited for optically thick cloud studies. Vertically integrated ice water pass (IWP) can be retrieved from space-based or airborne microwave and/or millimeter radiometer measurements [Vivekanandan *et al.*, 1991; Weng and Grody, 2000; Liu and Curry, 2000; Evans *et al.*, 2005]. To retrieve vertical ice water content (IWC) profiles of optically thick clouds, it is necessary to use cloud radar measurements. However, algorithms using single-wavelength radar spectrum moments have difficulties when applied to convective clouds [Matrosov *et al.*, 1994, 2002; Mace *et al.*, 2002], and retrievals by using simple empirical IWC-radar reflectivity

<sup>1</sup>Department of Atmospheric Science, University of Wyoming, Laramie, Wyoming, USA.

<sup>2</sup>NASA Goddard Space Flight Center, Greenbelt, Maryland, USA.

<sup>3</sup>Goddard Earth Sciences and Technology Center, University of Maryland Baltimore County, Baltimore, Maryland, USA.

<sup>4</sup>Also at NASA Goddard Space Flight Center, Greenbelt, Maryland, USA.

<sup>5</sup>National Centers for Atmospheric Research, Boulder, Colorado, USA.

factor ( $Z_e$ ) relationships may have uncertainties up to 100% [Sassen *et al.*, 2002].

[4] Algorithms based on multiwavelength radar measurements are so far the best choice for profiling optically thick ice clouds. Atlas and Ludlam [1961] first explored information contained in multiwavelength radar measurements for hail determination. Recently, multiwavelength radar measurements were used for cirrus studies by Matrosov [1993], Hogan and Illingworth [1999], and Hogan *et al.* [2000] and for optically thick ice clouds by Sekelsky *et al.* [1999]. In general, these algorithms used information contained in the measurements because of the different contributions of Rayleigh and Mie scattering at different wavelengths. These studies also indicated that the radar backscattering intensity of ice crystals in the Mie scattering region strongly depends on ice crystal shape, bulk density, size, and orientation. Because of lack of observations for justifying assumptions used in algorithm development, large uncertainties may be resulted in the retrievals and reducing these uncertainties is the major challenge of algorithm development based on multiwavelength radar measurements. The CRYSTAL-FACE field campaign 2002 provided us a rich data set to examine the necessary assumptions needed for the algorithm development, so that we can use more realistic assumptions to improve the accuracies of retrieved cloud properties.

[5] In this study, we will develop an algorithm to profile optically thick ice cloud microphysical properties by using airborne 9.6 and 94 GHz radar measurements from the NASA ER-2 high-altitude ( $\sim 20$  km) aircraft during the CRYSTAL-FACE field campaign. Compared with ground-based multiwavelength radar measurements, airborne measurements from the ER-2 avoid attenuation from moisture in the lower troposphere and precipitation often associated with deep ice clouds. These radars take advantage of higher radar sensitivity and higher-resolution measurements of upper tropospheric clouds since the cloud top is closer to the radar. The observational data are briefly introduced in section 2. The algorithm development is presented in section 3. In section 4, a case study is presented to show the capabilities of the algorithm. Comparisons of IWC and IWP from different approaches are given in section 5 to further illustrate advantages of using dual-wavelength radar measurements.

## 2. Observations

[6] During July 2002, the CRYSTAL-FACE field campaign was conducted by NASA. Six aircraft equipped with a variety of remote sensors and in situ probes provided comprehensive measurements of aerosol, clouds, and atmospheric chemistry over the south Florida and surrounding region. The data used in this study are from two radars that flew on the NASA ER-2 aircraft, and in situ size distribution and total condensed water content (CWC) measurements from the University of North Dakota Citation aircraft.

[7] The ER-2 Doppler radar (EDOP) is an X-band (9.6 GHz) Doppler radar mounted in the nose of a NASA ER-2. The instrument has two fixed antennas, one pointing at nadir and the second pointing approximately  $33^\circ$  ahead of nadir. This unique configuration enables EDOP to provide nadir measurements of reflectivity, vertical hydrometeor

motion (and vertical air motion  $w$  after fallspeed removal), and along-track wind ( $u$ ) and in the vertical plane mapped out by the ER-2. Additional details of the radar hardware and data processing are described by Heymsfield *et al.* [1996]. The cloud radar system (CRS) is a 94 GHz polarimetric Doppler radar developed for autonomous operation on a NASA ER-2 and for ground-based operation. On the ER-2, it is capable of detecting clouds and precipitation from the surface up to the aircraft altitude in the lower stratosphere. This radar is especially well suited for cirrus cloud studies because of its high sensitivity ( $-29$  dBZ<sub>e</sub> at 10 km range) and fine spatial resolution (e.g., 37.5 m in range). Its major data products include radar reflectivity, Doppler velocity, and velocity spectrum width. The details of the radar hardware and preliminary data are described by Li *et al.* [2004].

[8] EDOP has been used in many field experiments dealing with convection and hurricanes as well as for Tropical Rain Measuring Mission (TRMM) validation. However, during CRYSTAL-FACE, it was the first time that EDOP and CRS flew together on the ER-2. This provided a unique opportunity to study optically thick ice clouds from a dual-wavelength perspective. The calibration accuracy of CRS is  $\sim 1$  dB; EDOP has a similar accuracy. Since CRS and EDOP were collocated on the same aircraft, we verified the calibration by looking at cloud top, where ice particles are small and scattering at both wavelengths should be in the Rayleigh region. Therefore the Dual Wavelength Ratio (DWR) should have an accuracy slightly worse than the accuracy of the individual radars. Another main source of errors in the DWR is from mismatch of the EDOP and CRS beams. EDOP and CRS data from the CRYSTAL-FACE and other field campaigns are available at <http://meso-a.gsfc.nasa.gov/912/radar/>.

[9] The particle size distribution data used in this study were obtained from probes on the Citation aircraft that included the forward scattering spectrometer probe (FSSP), two-dimensional cloud probe (2D-C), two-dimensional precipitation probe (2D-P), high-volume precipitation spectrometer (HVPS) and the Cloud Particle Imager (CPI). The size distributions are merged from the 2D-C and the HVPS data sets [Heymsfield *et al.*, 2004] for a total of 15814 5-s size distributions. Among these size distributions, only 49 were within 3 km spatially and 200 s temporally of the EDOP and CRS measurements. However, these coincident size distributions and radar measurements provide important constraints for the equivalent radar reflectivity factor ( $Z_e$ ) calculations with the observed size distributions.

[10] Lacking accurate size information for small ice crystals introduces additional uncertainties in IWC calculated from size distribution data. According to the recent study by Heymsfield *et al.* [2005] based on CRYSTAL-FACE in situ data, the small particles contribute about 10–20% of the total IWC depending on the total IWC. We will use this result to approximately account for the contribution of small ice crystals in IWC estimations from size distributions. Because the  $Z_e$  calculation is more sensitive to larger particles than the IWC calculation, we will neglect the contribution of small ice crystals in the  $Z_e$  calculation.

[11] The CWC measured by the Counterflow Virtual Impactor (CVI) was also available from the Citation aircraft. Uncertainty for this CWC is estimated to be about 11% for a

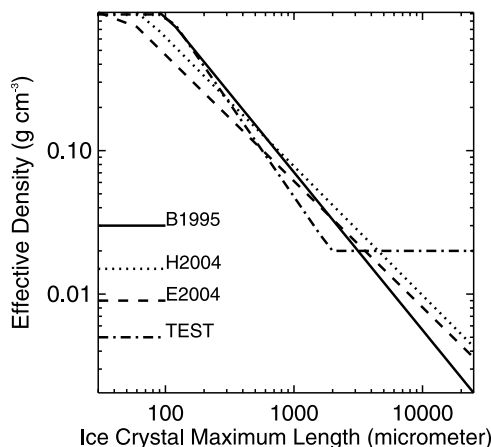


**Figure 1.** Ice crystal effective density as a function of ice crystal maximum length defined by different mass-length relationships. See text for more details.

CWC of  $0.2 \text{ g m}^{-3}$ , but increases for smaller CWC [Twohy *et al.*, 1997]. These measurements are important for constraining IWC calculated from measured size distributions. The in situ probes used here have sampling volumes ranging from  $0.004$  to  $1 \text{ m}^3 \text{ s}^{-1}$ . Therefore the radar sampling volume is at least 3 orders higher than those of in situ probes. The mismatched sampling volumes between the radar and the in situ measurements could be a serious issue for intercomparisons under situations of spatially inhomogeneous clouds.

[12] In addition, the NASA Compact Scanning Submillimeter Imaging Radiometer (CoSSIR) flew on the ER-2 aircraft, and operated with 12 channels from a frequency of 183 to 640 GHz. The main purpose of CoSSIR is for the retrieval of ice cloud properties [Wang *et al.*, 2001]. The CoSSIR measurements can be used to estimate ice water path (IWP) [Evans *et al.*, 2005]. The IWP retrieved from the CoSSIR will be used for comparison with the dual-wavelength algorithm discussed below. The IWP accuracies from the CoSSIR measurements depend on IWP values and are better than 30% for higher IWP values [Evans *et al.*, 2005].

### 3. Algorithm Development

#### 3.1. Forward $Z_e$ Calculation

[13] The forward calculation of  $Z_e$  from the measured or assumed size distributions is an important step for developing multiwavelength radar measurement algorithms [Matrosov, 1993; Hogan and Illingworth, 1999; Sekelsky *et al.*, 1999] or single-wavelength radar algorithms [Austin and Stephens, 2001; Wang and Sassen, 2002; Donovan *et al.*, 2004]. Calculation of  $Z_e$  from a given ice crystal size distribution defined in terms of ice crystal maximum length first requires an ice crystal mass-length relationship to estimate the ice mass of a given size ice crystal. Then  $Z_e$  can be estimated on the basis of the mass and size using appropriate scattering calculations. Different assumptions used in the forward calculations will result in uncertainties in developed algorithms. The CRYSTAL-FACE data are used here for providing more realistic assumptions in order to minimize the potential uncertainties caused by them.

[14] In this study, we use measured size distributions rather than assuming a general size distribution. Therefore the selection of a particle mass-length relationship is one of the major assumptions in the forward calculation. To determine the sensitivity to the mass-length relationship, we examine four mass-length relationships here. The first one is  $m = 2.94 \times 10^{-3} D^{1.9}$  (B1995) for aggregates of unrimed bullets, columns, and side planes developed by Locatelli and Hobbs [1974] and recommended by Brown and Francis [1995]. Units of  $m$  and  $D$  are  $\text{g}$  and  $\text{cm}$ , respectively. The second and third relations are derived from CRYSTAL-FACE data:  $m = 5.13 \times 10^{-3} D^{2.1}$  (H2004),  $m = 4.23 \times 10^{-3} D^{2.12}$  (E2004), by Heymsfield *et al.* [2004] and Evans *et al.* [2005], respectively. The ice crystal effective density can be defined as the total ice crystal mass divided by the volume of a sphere with the diameter of maximum ice crystal length. Therefore a mass-length relationship gives the effective density of ice crystals as a function of crystal size. According to Heymsfield *et al.* [2004], typical values for effective density range from near  $0.91 \text{ g cm}^{-3}$  for sub- $100\text{-}\mu\text{m}$  pristine ice crystals to near  $0.01 \text{ g cm}^{-3}$  for large aggregates. However, these power law relationships give very small effective density values for large ice crystals and effective density values larger than solid ice for small ice crystals. To avoid these limitations of a simple power law particle mass-length relationship, it is necessary to set the upper and lower limits of effective density values defined by a power law relationship or to use more complicated mass-length relationship formulation. Therefore we assume a mass-length relationship of  $m = 1.25 \times 10^{-3} D^{1.7}$  (TEST) and set the upper and lower limits of effective densities to  $0.89$  and  $0.02 \text{ g/cm}^3$ , respectively. These density bounds are based on the coincident in situ size distributions and radar measurements as discussed below. The ice crystal effective densities defined by these four relationships are presented in the Figure 1, and their differences among small and large size ice crystals are obvious.

[15] The particle mass-length relationships were developed originally for ice water content (IWC) estimations based on the measurements from ice particles sampled at the ground [Locatelli and Hobbs, 1974]. Therefore a mass-length relationship, which gives reasonable estimates of IWC, does not guarantee accurate  $Z_e$  estimations because  $Z_e$  is more sensitive to larger particles than IWC [Heymsfield *et al.*, 2005; Wang *et al.*, 2004]. Figure 2 shows the scatterplot of the IWC ratio between CVI measured and calculated using the four particle mass-length relationships given in Figure 1. To determine the contribution of small particles in the IWC calculation, we simply increase the calculated IWC by 15% according to the recent study of Heymsfield *et al.* [2005]. Though the values of IWC ratio have considerable scatter as indicated by large standard deviations of the mean ratios, these four relationships provide similar calculated IWC in terms of mean ratios. However, there can be a few dB differences in  $Z_e$  values while IWC calculations do not vary significantly by using different particle mass-length relationships [Wang *et al.*, 2004; Heymsfield *et al.*, 2005]. This point will be further illustrated below.

[16] When particle size is large compared with radar wavelength, we need to consider Mie scatter effects in the

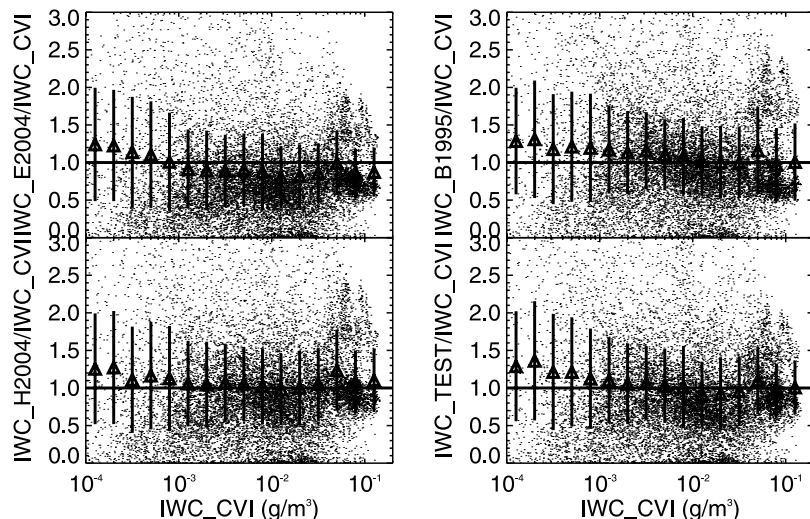


**Figure 2.** Ratio of calculated IWC with CVI measured as a function of CVI measured IWC. Each panel corresponds to a mass-length relationship given in Figure 1. The triangles and vertical bars represent means and standard deviations of the ratios within given IWC bins. Note the contribution of missed small ice crystals is assumed to be  $\sim 15\%$  of the total IWC on average.

$Z_e$  calculations. Studies have shown that the scattering by large ice crystals at radar wavelengths depends strongly on ice crystal size, shape and orientation [Matrosov, 1993; Liu and Illingworth, 1997; Hogan and Illingworth, 1999; Sekelsky et al., 1999; Hogan et al., 2000; Okamoto, 2002; Donovan et al., 2004]. For particles with the same mass and shape, the bulk densities of ice particles also affect the  $Z_e$  calculation. Therefore it is not an easy task to estimate the radar backscattering of irregular ice particles. This has become a major challenge for developing multiwavelength radar algorithms for ice clouds and solid precipitation. The results of T-Matrix calculations [Mishchenko and Travis, 1998] presented in Figure 3 simply illustrate the sensitivity of radar backscattering to these factors.

[17] The backscattering intensities of sphere and prolate spheroids with different bulk densities at 9.6 and 94 GHz are represented in Figure 3 as a function of the radius of the solid ice mass equivalent sphere ( $R_{solid}$ ). As indicated in Figure 3, the effects of Mie scatter and shapes at 9.6 GHz are small when  $R_{solid}$  of the ice crystal is smaller than  $\sim 1.5$  mm. Particles with this  $R_{solid}$  value are very large ice crystals in terms of ice crystal maximum length. However, different ice crystal shapes and bulk densities cause noticeable differences in the 94 GHz  $Z_e$  when  $R_{solid}$  is larger than  $\sim 0.2$  mm. In deep and/or optically thick ice clouds, most of ice crystals have sizes beyond 0.2 mm. These results are consistent with calculations using different shapes and scattering calculation techniques [Liu and Illingworth, 1997; Okamoto, 2002; Donovan et al., 2004].

[18] To retrieve ice crystal generalized effective size ( $D_{ge}$ , defined by Fu [1996]) and IWC from multiwavelength radar measurements, we need to rely on ice crystal backscattering intensity differences at different radar frequencies caused by Rayleigh and Mie scattering. Therefore we have to treat Mie scattering properly in order to have accurate retrievals. As illustrated in Figure 3, the 9.6 GHz  $Z_e$  calculation is only slightly affected by Mie scatter, and we need to consider Mie scattering at 94 GHz when particle length is larger than

a few hundred micrometers. The CRYSTAL-FACE data provide an opportunity to refine the  $Z_e$  calculation.

[19] On the basis of the above discussion, the selection of a mass-length relationship is a main factor affecting 9.6 GHz  $Z_e$  calculations. The impacts of different mass-length relationships on the 9.6 GHz  $Z_e$  calculation are

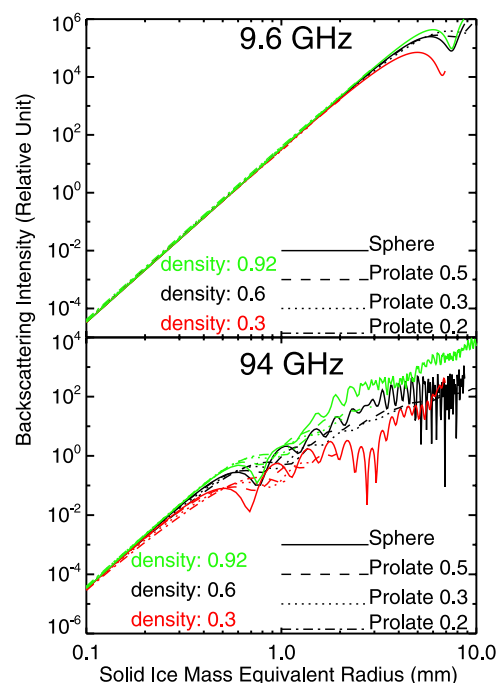


**Figure 3.** The 9.6 and 94 GHz backscattering intensities of different shape and bulk density ice crystals as a function of the radius of the solid mass equivalent ice sphere. Spheres and prolate spheroids with different aspect ratios are indicated by different line styles, and different bulk densities are shown with different colors.

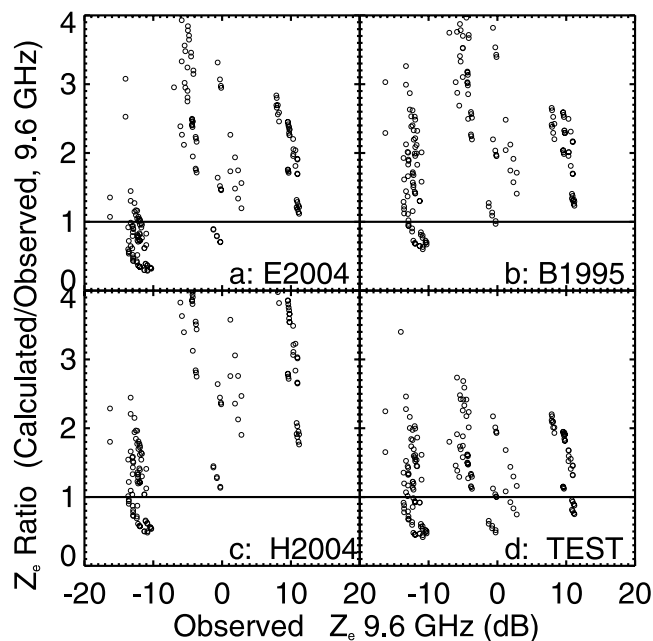


**Figure 4.** Ratios of calculated and observed 9.6 GHz  $Z_e$  as a function of observed 9.6 GHz  $Z_e$  for four different mass-length relationships given in Figure 1 based on coincident observations.

shown in Figure 4 based on coincident in situ particle size distributions and radar measurements. There is a large variation of the ratio between calculated  $Z_e$  and EDOP-measured  $Z_e$  for each relationship. This highlights the difficulties of intercomparing ice cloud in situ measurements with radar measurements since sample volumes are totally different and the measurements may differ because of ice cloud spatial inhomogeneity. However, there are noticeable differences among different particle mass-length relationships. It is clear that the mean  $Z_e$  ratios of B1995, E2004, and H2004 increase with the increase of observed  $Z_e$ . This bias is partly corrected by the TEST relationship. The differences among them are mainly caused by distributing ice mass differently among different size particles. On the basis of this comparison, we conclude that the TEST relationship gives a better 9.6 GHz  $Z_e$  calculation.

[20] As indicated in Figure 3, it is more complicated to calculate 94 GHz  $Z_e$ . Given a mass-length relationship, we know the mass of an ice particle from its size. In the Mie scattering regime, we also need to know the ice particle shape and bulk density in order to calculate accurate 94 GHz  $Z_e$ . Although the backscatter of simple shape ice crystals can be calculated accurately at radar wavelengths [Matrosov, 1993; Aydin and Tang, 1997; Okamoto, 2002], it is difficult to choose an ice crystal shape or an ensemble of shapes that represent the general nonspherical effects of the variety of ice crystal shapes in ice clouds. Donovan *et al.* [2004] indicated that the equivalent area or equivalent mass solid ice sphere representation for irregular particles performs well compared with the discrete-dipole approximation (DDA) calculation for ice crystal size below 1000  $\mu\text{m}$ . In general, we still do not have sufficient knowledge to accurately account for both the shape and density effects of large ice crystals on the 94 GHz  $Z_e$  calculation. Here, we

search for a simple but effective approach to reasonably take both effects into account by using CRYSTAL-FACE data.

[21] Similar to the 9.6 GHz  $Z_e$  calculation, we use coincident in situ and radar observations to guide the 94 GHz  $Z_e$  calculation [Wang *et al.*, 2004]. However, coincident data are very limited and mainly occurs when 9.6 GHz  $Z_e$  values are below 10 dBZ. One way to overcome these limitations is to compare statistical relationships obtained from the radar data and from in situ size distributions by assuming that both sources of information provide a typical sampling of the cloud systems. Figure 5 presents a frequency distribution of DWR between 9.6 and 94 GHz as a function of 9.6 GHz  $Z_e$  based on CRYSTAL-FACE observations. For a given 9.6 GHz  $Z_e$ , there is a wide distribution of DWR. This clearly indicates that the ice crystal size distributions are varying widely in nature; therefore it is difficult to estimate IWC from a single-wavelength radar  $Z_e$  measurement.

[22] Simple approximations for irregular ice crystals are to use different equivalent spheres to calculate the particle scattering properties [Donovan *et al.*, 2004; Liu, 2004]. The first approach tested here is to convert the total ice crystal mass estimated from the mass-length relationship into a solid sphere. The second approximation is to assume an ice-air mixture sphere with a diameter of the maximum particle length and total ice crystal mass. Calculated DWRs as a function of calculated 9.6 GHz  $Z_e$  for these two approaches are given in Figures 6a and 6b. The solid line is the observed mean DWR- $Z_e$  relationship discussed in Figure 5. It is clear that the first approach produces much smaller DWR than the observed and the second approach produces a larger DWR than the observed when 9.6 GHz  $Z_e$  is above 20 dB. Smaller solid equivalent spheres used in the first approach introduce a weak Mie scatter effect and therefore overestimate 94 GHz  $Z_e$ . On the other hand, larger size

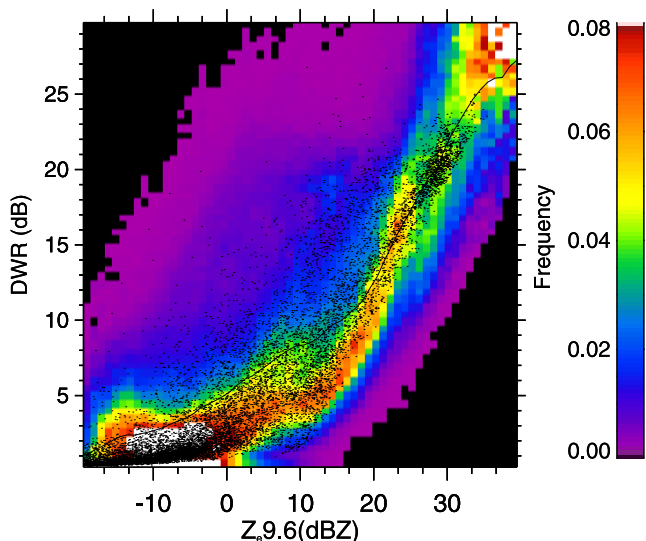


**Figure 5.** DWR- $Z_e$  relationship based on CRS and EDOP observations during the CRYSTAL-FACE. The solid line represents the mean DWR within given 9.6 GHz  $Z_e$  bins whereas the black dots are calculated results based on the in situ size distributions.

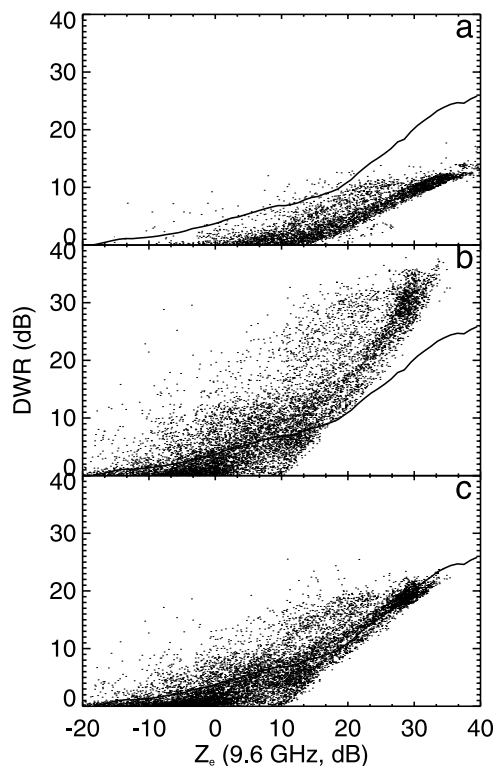


**Figure 6.** Calculated DWR- $Z_e$  relationships from three different approaches: (a) assuming a mass-equivalent solid sphere, (b) assuming an ice-air mixture sphere with a diameter of the maximum particle length, and (c) using a fixed density for large ice crystal (see text for additional information). The solid line represents the mean relationship observed from CRYSTAL-FACE.

spheres used in the second approach introduce a strong Mie scattering effect and underestimate 94 GHz  $Z_e$ .

[23] Figures 6a and 6b suggest that an approach assuming a spherical ice particle with size and bulk density between first and second approaches may be appropriate. To test his idea, the second approach is modified by fixing the bulk density of particles with a maximum length larger than  $2800 \mu\text{m}$  to be  $0.2 \text{ g cm}^{-3}$ . Liu [2004] suggested a similar approach for a high microwave frequency application. This modification approximates the large particles with smaller size and higher bulk density equivalent spheres than those used in the second approach. According to the calculations given in Figure 3, this modification for large particles can reduce the Mie scattering effects in the  $Z_e$  calculations. The calculated DWR and 9.6 GHz  $Z_e$  with this approach are given in Figure 6c, which shows a better agreement with the observed mean relationship. The calculations with this approach are also over plotted in Figure 5 (scatter black dots) and have good agreement with the observed DWR frequency distributions.

[24] DWR is the main parameter used to retrieve cloud microphysical properties from dual-wavelength radar measurements. The above discussion indicates that the third approach can provide a reasonably good DWR calculation, at least from a statistical point of view. Therefore we use this approach for  $Z_e$  calculations. To

further evaluate this approach, Figure 7 shows the IWC ratio, the ratio of the calculated IWC and the CVI measured IWC, as functions of the 9.6 GHz  $Z_e$  and the DWR. Each point corresponds to a 5-s average in situ size distribution. To illustrate trends better, the averaged IWC ratios for given  $Z_e$  or the DWR bins are plotted with triangle symbols, and the solid line represents an IWC ratio of one. Although the individual ratios have considerable scatter, the mean ratio is very close to one over a wide range of  $Z_e$  and DWR. The comparison of calculated  $Z_e$  and observed  $Z_e$  for coincident observations is given in Figure 8. The calculated and observed  $Z_e$  are scattered around the 1:1 line with most of points within  $\pm 3 \text{ dB}$  of this line. These results not only show that our IWC calculations based on size distributions have good accuracy, but it also illustrates that the approaches used here for  $Z_e$  calculations are reliable.

### 3.2. Retrieval of Ice Cloud Microphysical Properties

[25] With the above discussions, we are able to develop relationships among IWC,  $D_{gc}$ ,  $Z_e$  and DWR with confidence. The mean ratio of 9.6 GHz  $Z_e$  to IWC as function of DWR is presented in Figure 9a. The standard deviation values are within  $\sim 30\%$  of the mean value, and this reflects the natural variations of cloud properties and uncertainties resulting from the assumptions. Here, we use the mean relationship to retrieve IWC from 9.6 GHz  $Z_e$  and DWR. As shown in Figure 8, there are almost no IWC biases in terms

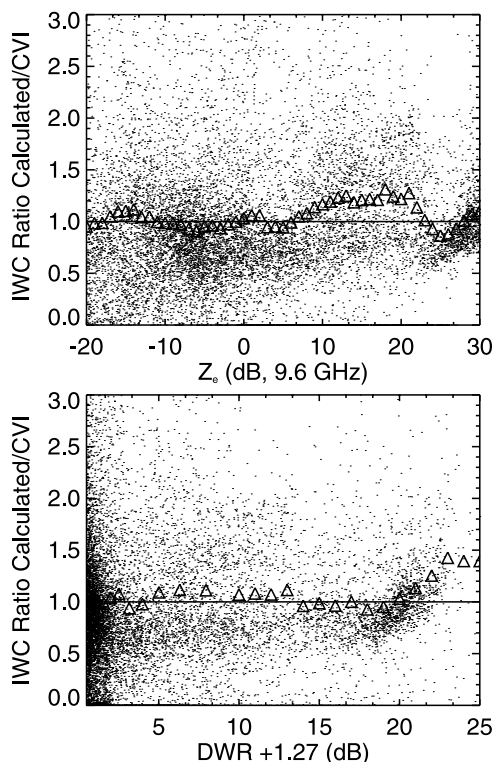


**Figure 7.** IWC ratio of calculated and CVI measured as functions of 9.6 GHz  $Z_e$  and DWR between 9.6 and 94 GHz. The solid lines indicate the ratio of 1, and triangles represent mean ratios within given bin sizes. The 1.27 dB reflects the difference between 9.6 GHz and 94 GHz  $Z_e$  in Rayleigh scattering regions.

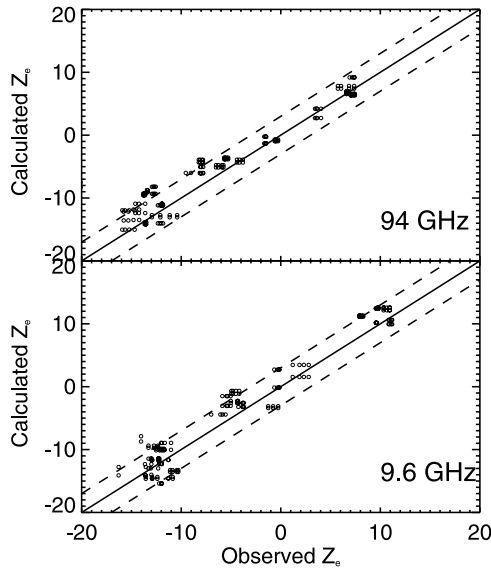


**Figure 8.** Comparison of calculated  $Z_e$  with observed  $Z_e$  at 9.6 and 94 GHz for collocated radar and in situ observations. The solid line is the 1:1 line, and the dashed lines indicate a  $\pm 3$  dB region about the 1:1 line.

of DWR and 9.6 GHz  $Z_e$ . Therefore we simply use these standard deviations to estimate the retrieval uncertainty of IWC. The approach used here is simple compared to more systematic treatments of retrieval errors [Austin and Stephens, 2001; Mace et al., 2002; Evans et al., 2005]. However, the standard deviation statistics should provide reasonable estimates of statistical uncertainties, and they are readily applied to the observations.

[26] There is a  $\sim 1.27$  dB difference between 9.6 GHz and 94 GHz  $Z_e$  in Rayleigh scattering regions due to their different water dielectric constants. Therefore 1.27 is added to DWR for fitting the ratio of 9.6 GHz  $Z_e$  to IWC as function of DWR. The fitted relationship is  $y = a + bx + cx^2$ , where  $x = \log(DWR + 1.27)$ ,  $y = \ln(10^{0.723} Z_e / IWC)$ , and  $a$ ,  $b$ , and  $c$  are constants. The values for  $a$ ,  $b$ , and  $c$  are 2.59324, 3.17094, and 0.137975; 3.00510, 0.337015, and  $-0.00263462$  for  $DWR + 1.27 \leq$  and  $> 7.94328$  dB, respectively. The relative uncertainty of observed DWR increases when DWR is below  $-0.5$  dB; this will also increase the retrieved IWC uncertainty. Small DWR regions are usually located in the upper regions of clouds where particle sizes are relatively small and can be detected by the Cloud Physics Lidar (CPL) on the ER-2. Combining CPL and CRS measurements covers the overlap regions that may not be detected by the 9.6 GHz EDOP radar [Wang and Sassen, 2002]. In the current retrieval, we do not apply the dual-wavelength approach when DWR is below  $-0.5$  dB, and instead we use a  $Z_e$ -IWC relationship to obtain IWC in this situation. In the future, we will combine CRS and CPL measurements to cover this region.

[27] Similarly, we can develop a relationship between  $D_{ge}$  and DWR. We use the general definition of  $D_{ge}$  given by Fu [1996]:

$$D_{ge} = \frac{2}{\sqrt{2\rho_i}} \frac{IWC}{A_c}, \quad (1)$$

where  $A_c$  is the cross-sectional area of ice crystals per unit volume and  $\rho_i$  is solid ice density. By using the cross-sectional area of ice cloud particles parameterized by Heymsfield and Miloshevich [2003], we can calculate  $A_c$  from the measured size distributions and then combine this IWC to derive  $D_{ge}$ . According to Heymsfield and Miloshevich [2003], the  $A_c$  of ice crystal depends on ice crystal shape as well as ice crystal length. Like the IWC calculations from in situ size distributions, the uncertainty for the  $D_{ge}$  calculation for a given size distribution is also large. However, the mean properties of  $D_{ge}$  from a large data set should have a better accuracy from a statistical point of view. The mean  $D_{ge}$  as a function of DWR is presented in Figure 9b and it is used to develop relationship between  $D_{ge}$  and DWR for the retrieval. Similar to the IWC retrieval, we use the standard deviation of mean  $D_{ge}$  to characterize the  $D_{ge}$  retrieval uncertainty.

[28] For optically thick ice clouds, we also need to consider the attenuation by ice crystals at 94 GHz. Because of the strong Mie scattering effect at 94 GHz, it is challenging to correct for attenuation properly when only 94 GHz measurements are available. For dual-wavelength measurements, a simple approach is to use the 9.6 GHz  $Z_e$  to estimate 94 GHz attenuation. Figure 10 shows one way 94 GHz attenuation coefficients as a function of 9.6 GHz  $Z_e$  based on CRYSTAL-FACE in situ size distributions. When 9.6 GHz  $Z_e$  is below 15 dBZ, there is a wide range of attenuation coefficients at 94 GHz. Fortunately, the attenuation coefficient is relatively small for this  $Z_e$  range; therefore we can use mean attenuation coefficients for the attenuation correction. The main purpose for correcting the

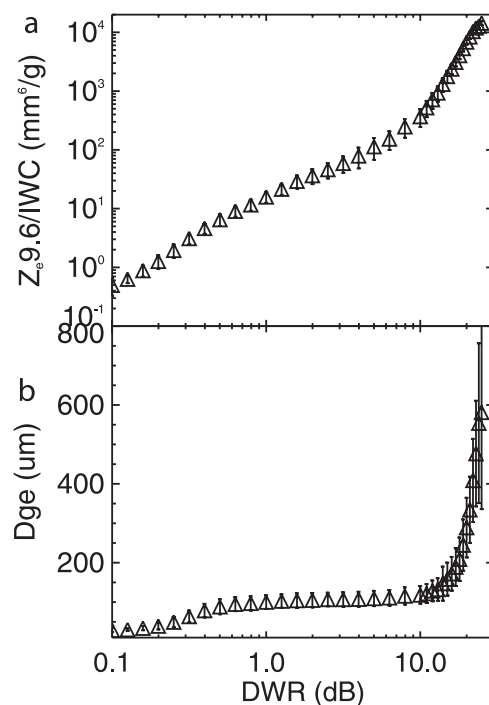


**Figure 9.** Mean and standard deviation of (a) IWC and (b)  $D_{ge}$  as a function of DWR between 9.6 and 94 GHz calculated on the basis of all in situ size distribution data from the CRYSTAL-FACE. The vertical bars indicate the standard deviation about the mean.

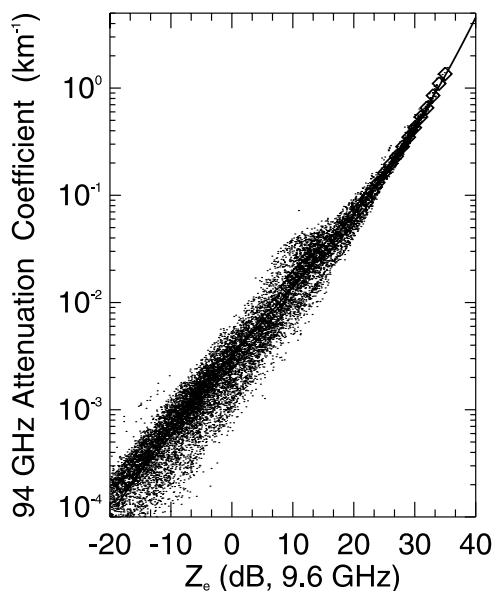


**Figure 10.** The 94 GHz attenuation coefficient of ice clouds as a function of  $Z_e$  at 9.6 GHz. The mean attenuation coefficients for different  $Z_e$  bins are represented by diamonds. The solid line is the fitted result of mean values.

94 GHz attenuation is to obtain a better DWR estimate that will improve the IWC retrieval accuracy, especially near convective regions. First, the 94 GHz cloud extinction coefficients at height  $H$ ,  $\sigma(H)$ , are estimated by using the curve fitted to the mean values shown in Figure 10. Then, the 94 GHz  $Z_e$  can be corrected by multiplying the factor,

$e^{2 \int_H^{H_{top}} \sigma(h) dh}$ , where  $H_{top}$  is the cloud apparent top height from radar measurements.

#### 4. Case Study

[29] To demonstrate the retrieval algorithm capability and its potential applications, we present cross sections from three flight lines across a convective system observed on 29 July 2002 during CRYSTAL-FACE. Figure 11 displays a sequence of GOES 8 IR channel ( $10.8 \mu\text{m}$ ) images observed on 29 July 2002 during these flight lines. In each GOES image, the flight track closest to the image time (solid black lines) and its time period are indicated. The GOES images clearly indicate the development of the cloud systems during the ER-2 flight. The two sea breeze initiated convective regions initially developed from the east and west shores of the southern Florida around 1700 UTC, then the anvils from each convective system merged after 1930 UTC as the systems matured. After 2030 UTC, we cannot separate the two convective cells in the GOES IR image. The ER-2 measurements were mainly focused on the westernmost convective region as indicated by the flight tracks.

[30] The CRS and EDOP  $Z_e$  measurements from the ER-2 (Figures 12a–12f) provide unique vertical cross sections through the convective region for three selected time periods (1942–1959, 2023–2040, and 2043–2101 UTC). The corresponding DWR structures are plotted in Figures 12g–12i. These sections cut through a decaying region of the convection that appears as a deep ice region aloft with light rain near the surface. The DWR plots clearly indicates strong Mie scattering in the lower part of the ice cloud region. Because the ice crystal size usually increases with decreasing height, this is evidenced by the similar behavior of DWR in

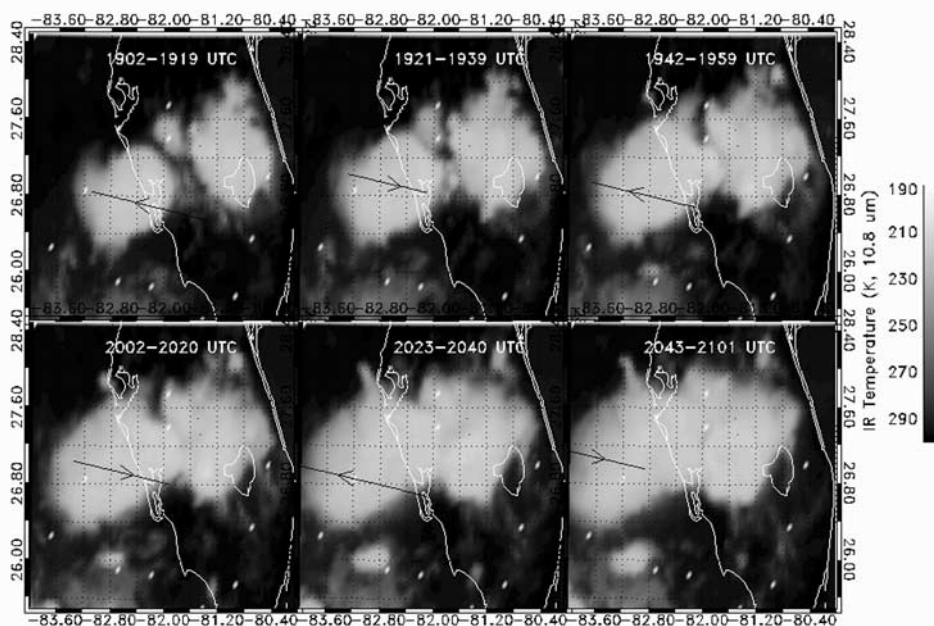


**Figure 11.** GOES IR images with ER-2 flight tracks (solid lines) during six periods observed on 29 July 2002 over the west coast of Florida. The solid lines over cloud decks are ER-2 flight tracks with arrows indicating the flight direction.

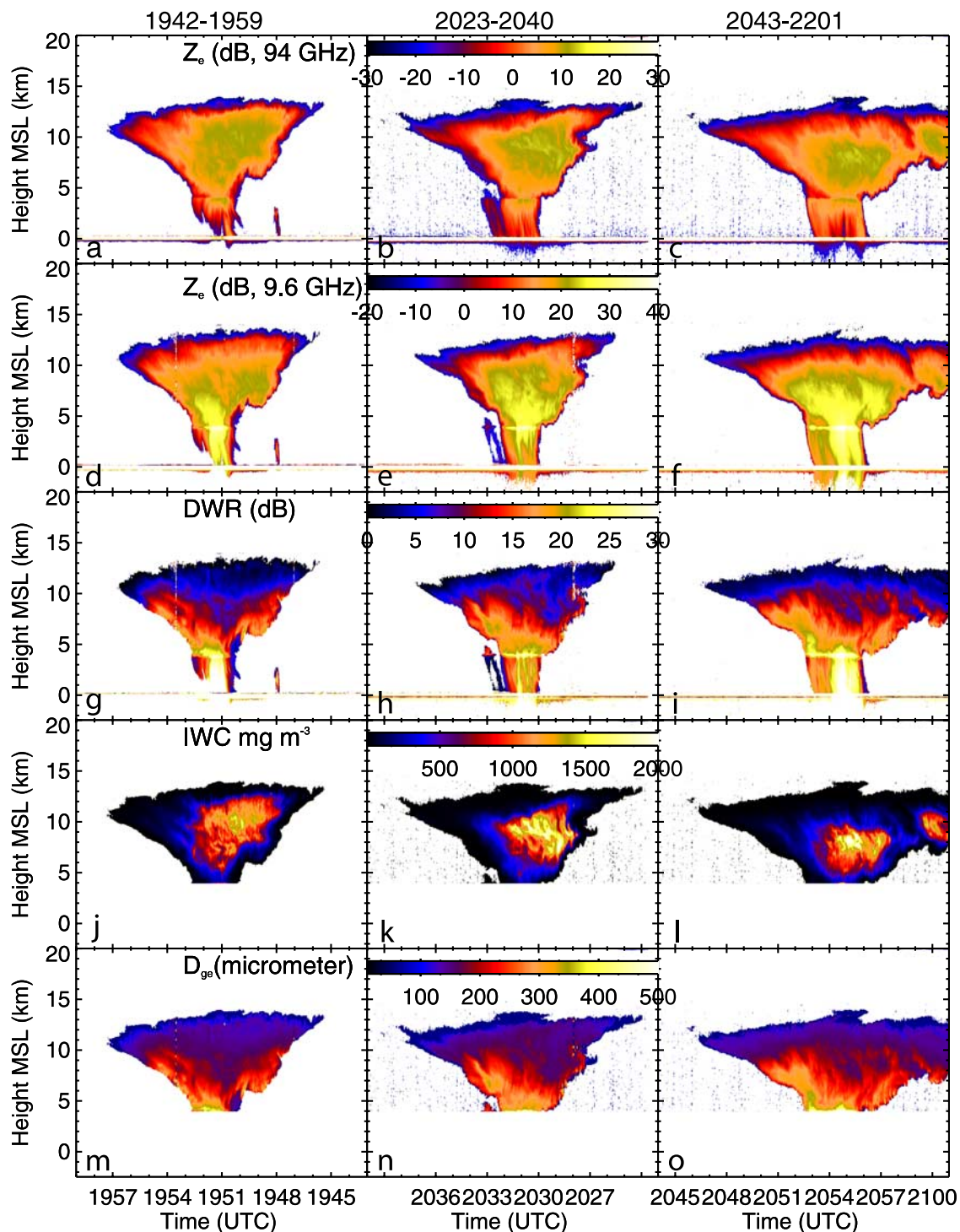


**Figure 12.** Time-height cross sections of observed (a–c) 94 and (d–f) 9.6 GHz  $Z_e$ , (g–i) DWR, and (j–l) retrieved IWC and (m–o)  $D_{ge}$  for three flight tracks given in Figure 11. Each column represents a flight track with time period given at the top. Note the color scales are different for 94 and 9.6 GHz  $Z_e$ . The cross sections are plotted in the same east-to-west orientation with west on the left side.

Figures 12g–12i. The bright band at approximately the freezing level altitude is evident in the 9.6 GHz observations, and the dual-wavelength approach discussed above can be used for the retrieval of ice cloud microphysical properties above the bright band. However, this approach would not be useful for the initial developing stage of convective clouds

because of the potential existence of significant amount of supercooled water above freezing level, which can result in strong attenuation at 94 GHz.

[31] The retrieved IWC and  $D_{ge}$  images presented in Figures 12j–12o show interesting evolution of the microphysical structure. Though this may be partially caused by

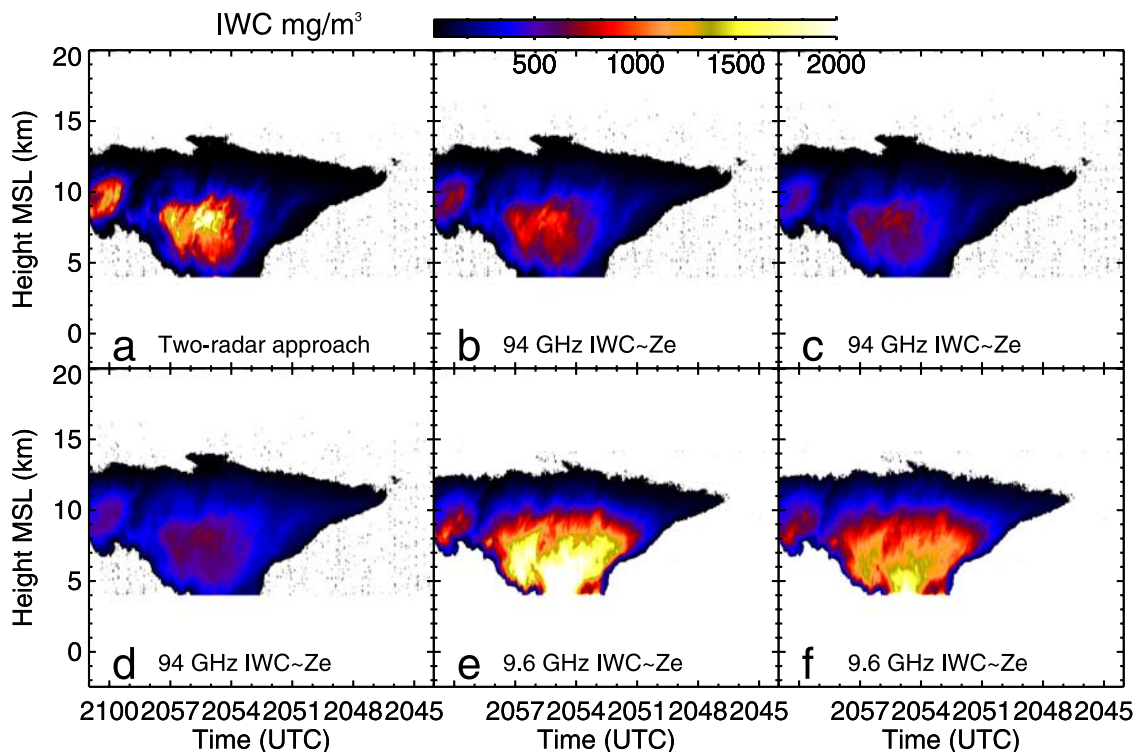


**Figure 13.** IWC comparison from different approaches: (a) dual-wavelength radar approach discussed in this paper; 94 GHz Z-IWC relationships of (b) *Liu and Illingworth* [2000], (c) *Matrosov et al.* [2003], and (d) *Heymsfield et al.* [2005]; and 9.6 GHz Z-IWC relationships of (e)  $IWC = 0.097 \cdot Z_e^{0.5}$  and (f) *Heymsfield et al.* [2005].

the position of the flight track relative to the storm center, the differences appear to be mostly related to the storm-scale dynamics and cloud physics processes. The larger convectively generated particles fall out first since they have higher fallspeeds; therefore large particles are mainly located near the cloud base as revealed by  $D_{ge}$  images (Figure 12m–12o). Interestingly, the higher-IWC regions usually correspond to regions with smaller particles. The data suggest that large ice particles were initially released aloft by a convective anvil, and then these particles sedimented out of the cloud. There is a noticeable decrease in the height and size of the high-IWC region between the first and third flight line, a period of about 1 hour. By the third flight line, the drizzle below the cloud layer strengthens as the larger particles sediment out. In future research, combining these retrievals with other observations and model simulations are needed to further understand the storm structure and its evolution.

## 5. IWC and IWP Comparison With the Other Approaches

[32] The case study in last section illustrates the excellent microphysical profiling capability by combining CRS and EDOP measurements. The IWC comparison given in Figure 13 further illustrates the advantage of using dual-wavelength radar measurements (Figure 13a) compared with single-wavelength radar measurements (Figures 13b–13f). For single-wavelength radar measurements, we can use IWC- $Z_e$  relationships to estimate the IWC profile

[*Sassen, 1987; Liu and Illingworth, 2000*]. However, the uncertainties in IWC from these relationships can be over 100% when they are applied to situations significantly different from the data sets they were derived from [*Sassen et al., 2002*]. Here three single-wavelength 94 GHz IWC- $Z_e$  relationships are used for comparison:  $IWC = 0.137 Z_e^{0.643}$  (L2000, Figure 13b) proposed by *Liu and Illingworth* [2000],  $IWC = 0.11 Z_e^{0.63}$  (M2001, Figure 13c) proposed by *Matrosov et al.* [2003], and  $Z_e = 4.0 IWC^{1.58}$  ( $IWC < 0.059 \text{ g m}^{-3}$ ) and  $Z_e = 54.8 IWC^{2.5}$  ( $IWC > 0.059 \text{ g m}^{-3}$ , Figure 13d) proposed by *Heymsfield et al.* [2005]. According to *Sassen et al.* [2002], the first two relationships perform well for cirrus clouds. Two relationships for 9.6 GHz are used: (1)  $IWC = 0.097 Z_e^{0.5}$  (Figure 13e) and (2)  $Z_e = 8.9 IWC^{1.66}$  ( $IWC < 0.059 \text{ g m}^{-3}$ ) and  $Z_e = 178.6 IWC^{2.72}$  ( $IWC > 0.059 \text{ g m}^{-3}$ , Figure 13f) proposed by *Heymsfield et al.* [2005]. Figure 13 suggests that the IWC- $Z_e$  relationships for the same radar wavelength give similar IWC structure, and there are big differences between 9.6 and 94 GHz relationships. Compared with the retrievals by the dual-wavelength radar approach (Figure 13a), the IWC- $Z_e$  relationships for 94 GHz underestimate high IWC and the IWC- $Z_e$  relationships for 9.6 GHz overestimate IWC. For this case, the 94 GHz measurements provide a more realistic vertical IWC structure. The difference between 9.6 and 94 GHz is mainly caused by the strong Mie scattering effects observed at 94 GHz.

[33] One way to evaluate the performance of the dual-wavelength algorithm is to compare vertically integrated ice water path (IWP) obtained by CoSSIR. Figure 14 presents

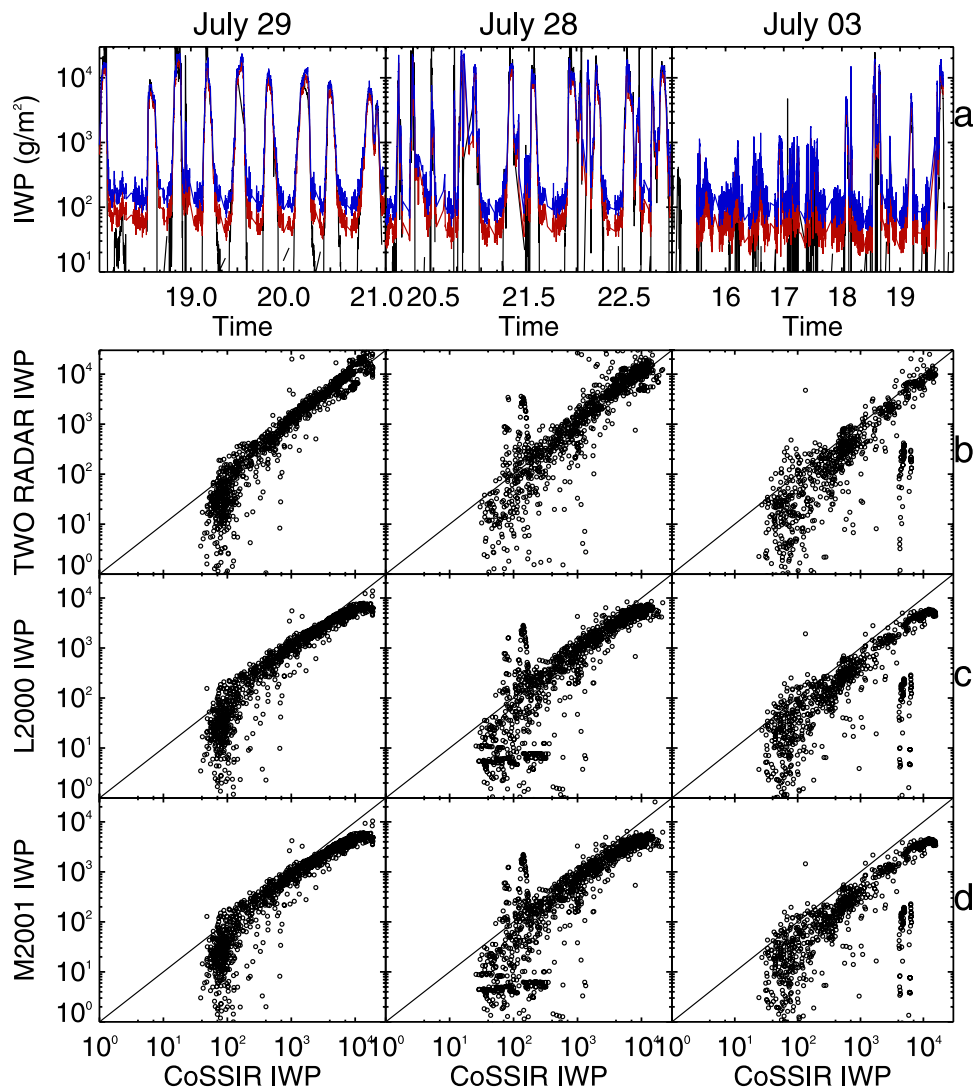


**Figure 14.** (a–d) Intercomparison of IWP derived from the dual-wavelength radar approach, CoSSIR, and two  $Z_c$ -IWC relationships based on measurements on 3, 28, and 29 July 2002 during the CRYSTAL-FACE. Figure 14a is for IWP time series of CoSSIR (red lines), dual-wavelength approach (black line), and CoSSIR retrieval + uncertainty (1 sigma) (blue lines).

an intercomparison of IWPs retrieved from the CoSSIR nadir measurements [Evans *et al.*, 2005], the dual-wavelength radar measurements, and those estimated using IWC- $Z_c$  relationships. Although CoSSIR measurements are unable to provide an accurate IWC profile, they can be used to retrieve reliable IWP [Evans *et al.*, 2005]. Three columns in Figure 14 represent three different days, and from left to right are for 29, 28, and 3 July, respectively. The time series of IWP from CoSSIR and dual-wavelength retrievals are compared in row “a”. There is good agreement between them when IWP values are larger than 100 g m<sup>-2</sup>. The scatterplots comparing CoSSIR IWP with IWPs from dual-wavelength approach, and two  $Z_c$ -IWC relationships are given in rows “b” to “d”. The limitation of current CoSSIR measurements for retrieval of small IWP is clear in the scatterplots. Figure 14b indicates a good correlation between CoSSIR IWP and dual-wavelength derived IWP from 100 up to 20000 g m<sup>-2</sup>. However, IWPs derived from the IWC- $Z_c$  relationships (L2000 and M2001) only have a good correla-

tion with CoSSIR IWP from 100 up to 1000 g m<sup>-2</sup>, then begin to underestimate IWP above 1000 g m<sup>-2</sup>. The consistency between the IWP derived from CoSSIR measurements and from the dual-wavelength radar measurements suggests some validity to the dual-wavelength approach developed here. This intercomparison also clearly indicates the advantage of dual-wavelength radar approach over simple IWC- $Z_c$  relationships.

## 6. Summary

[34] An algorithm using the EDOP and CRS measurements from the ER-2 aircraft is developed to retrieve optically thick ice cloud microphysical property profiles. For algorithm development, we need to accurately calculate the 9.6 and 94 GHz  $Z_c$  from the observed in situ size distributions. According to scattering calculations, 94 GHz  $Z_c$  is more sensitive to ice crystal shapes, size, and bulk density than 9.6 GHz  $Z_c$ . The coincident in situ size

distribution data and radar measurements obtained during the CRYSTAL-FACE field campaign provide a unique chance to refine the calculations of 9.6 and 94 GHz  $Z_e$ . With the guidance of observations, we selected a particle mass length relationship to provide a better 9.6 GHz  $Z_e$  calculation, and developed a simple approach to account for Mie scatter and nonspherical effects in the 94 GHz  $Z_e$  calculation.

[35] The results clearly indicated that assumptions and approximations used in the algorithm development provide unbiased IWC estimation in larger ranges of DWR and 9.6 GHz  $Z_e$  by comparing with CVI measured IWC. The observational constraints give us a higher confidence in the developing relationships for IWC and  $D_{gc}$  retrievals. Mean relationships between IWC and  $D_{gc}$  with DWR and 9.6 GHz  $Z_e$  are developed and used for IWC and  $D_{gc}$  retrievals. The standard deviations of mean values are used to estimate retrieval uncertainties. The developed relationships may be not universal, and we will refine them with more data from other field experiments. To improve DWR estimation from 94 and 9.6 GHz  $Z_e$  measurements, ice cloud attenuation at 94 GHz is approximately corrected by using unattenuated 9.6 GHz measurements.

[36] The capability of the approach is illustrated with a decaying convective region observed during CRYSTAL-FACE. With the airborne dual-wavelength radar measurement, we are able to provide high-spatial resolution cloud microphysical properties, which are not possible from in situ sampling at a single altitude and from single-wavelength radar measurements. The good agreement between IWPs derived from the dual-wavelength approach and from CoSSIR measurements indicates reasonable accuracy of our IWC retrievals. The case study also shows that this kind of airborne profiling capability provides important information to study the evolution of convective clouds and other optically thick ice clouds. The high-resolution cloud microphysical properties also provide a more effective way to compare the radar observations with cloud resolving model simulations. In the future, we will combine cloud retrievals with other observations and model simulations to better understand cloud physics and dynamics. The retrieved results have many other applications, for example, providing a database for passive remote sensing algorithm development and for improving the CloudSat retrieval for optically thick ice clouds.

[37] **Acknowledgments.** This work was supported by the NASA Radiation Sciences Program under the CRYSTAL-FACE funding 622-45-06. Z. Wang's participation was also supported by the NASA CloudSat mission and DOE grant DE-FG02-03ER63536 from the Atmospheric Radiation Measurement Program. We are grateful to Frank Evans of University of Colorado for providing the CoSSIR IWP retrievals. We are appreciative of the help from Lin Tian of Goddard Earth Science and Technology Center and Larry Belcher of Science Systems and Applications, Inc., for the radar data processing and other issues related to the data.

## References

- Atlas, D., and F. H. Ludlam (1961), Multi-wavelength radar reflectivity of hailstorms, *Q. J. R. Meteorol. Soc.*, **87**, 523–534.
- Austin, R. T., and G. L. Stephens (2001), Retrieval of stratus cloud microphysical parameters using millimetric radar and visible optical depth in preparation for CloudSat: 1. Algorithm formulation, *J. Geophys. Res.*, **106**, 28,233–28,242.
- Aydin, K., and C. Tang (1997), Relationships between IWC and polarimetric measurements at 94 and 220 GHz for hexagonal columns and plates, *J. Atmos. Oceanic Technol.*, **14**, 1055–1063.
- Brown, P. R. A., and P. N. Francis (1995), Improved measurements of the ice water content in cirrus using a total-water probe, *J. Atmos. Oceanic Technol.*, **12**, 410–414.
- Donovan, D. P., and A. C. A. P. Van Lammeren (2001), Cloud effective particle size and water content profile retrievals using combined lidar and radar observations: 1. Theory and examples, *J. Geophys. Res.*, **106**, 27,425–27,448.
- Donovan, D. P., M. Quante, I. Schlimme, and A. Macke (2004), Use of equivalent spheres to model the relation between radar reflectivity and optical extinction of ice cloud particles, *Appl. Opt.*, **43**, 4929–4940.
- Evans, K. F., J. R. Wang, P. E. Racette, G. M. Heymsfield, and L. Li (2005), Ice cloud retrievals and analysis with the compact scanning submillimeter imaging radiometer and the cloud radar system during CRYSTAL FACE, *J. Appl. Meteorol.*, **44**, 839–859.
- Fu, Q. (1996), An accurate parameterization of the solar radiative properties of cirrus clouds for climate models, *J. Clim.*, **9**, 2058–2082.
- Heymsfield, A. J., and L. M. Miloshevich (2003), Parameterizations for the cross-sectional area and extinction of cirrus and stratiform ice cloud particles, *J. Atmos. Sci.*, **60**, 936–956.
- Heymsfield, A. J., A. Bansemmer, C. Schmitt, C. Twohy, and M. R. Poellot (2004), Effective ice particle densities derived from aircraft data, *J. Atmos. Sci.*, **61**, 982–1003.
- Heymsfield, A. J., Z. Wang, and S. Matrosov (2005), Improved radar ice water content retrieval algorithms using coincident microphysical and radar measurements, *J. Appl. Meteorol.*, in press.
- Heymsfield, G. M., S. W. Bidwell, I. J. Caylor, A. S. S. Nicholson, W. C. Bonczyk, L. Miller, D. Vandemark, P. E. Racette, and L. R. Dod (1996), The EDOP radar system on the high-altitude NASA ER-2 aircraft, *J. Atmos. Oceanic Technol.*, **13**, 795–809.
- Hogan, R. J., and A. J. Illingworth (1999), The potential of spaceborne dual-wavelength radar to make global measurements of cirrus clouds, *J. Atmos. Oceanic Technol.*, **16**, 518–531.
- Hogan, R. J., A. J. Illingworth, and H. Sauvageot (2000), Measuring crystal size in cirrus using 35 and 94 GHz radars, *J. Atmos. Oceanic Technol.*, **17**, 27–37.
- Li, L., G. M. Heymsfield, P. E. Racette, T. Lin, and E. Zenker (2004), A 94 GHz cloud radar system on a NASA high-altitude ER-2 aircraft, *J. Atmos. Oceanic Technol.*, **21**, 1378–1388.
- Liou, K. N. (1986), Influence of cirrus clouds on weather and climate processes: A global perspective, *Mon. Weather Rev.*, **114**, 1167–1199.
- Liu, C.-L., and A. J. Illingworth (1997), Error analysis of backscatter from discrete dipole approximation for different particle shapes, *Atmos. Res.*, **44**, 231–241.
- Liu, C., and A. J. Illingworth (2000), Toward more accurate retrievals of ice water content from radar measurements of clouds, *J. Appl. Meteorol.*, **39**, 1130–1146.
- Liu, G. (2004), Approximation of single scattering properties of ice and snow particles for high microwave frequencies, *J. Atmos. Sci.*, **61**, 2441–2456.
- Liu, G., and J. A. Curry (2000), Determination of ice water path and mass median particle size using multichannel microwave measurements, *J. Appl. Meteorol.*, **39**, 1318–1329.
- Locatelli, J. D., and P. V. Hobbs (1974), Fall speeds and masses of solid precipitation particles, *J. Geophys. Res.*, **79**, 2185–2197.
- Lynch, D. K., K. Sassen, A. Del Genio, A. Heymsfield, P. Minnis, M. Platt, M. Quante, U. Schumann, and H. Sundqvist (2002), Cirrus: The future, in *Cirrus*, edited by D. Lynch et al., pp. 449–455, Oxford Univ. Press, New York.
- Mace, G. G., A. J. Heymsfield, and M. R. Poellot (2002), On retrieving the microphysical properties of cirrus clouds using the moments of the millimeter-wavelength Doppler spectrum, *J. Geophys. Res.*, **107**(D24), 4815, doi:10.1029/2001JD001308.
- Matrosov, S. Y. (1993), Possibilities of cirrus particles sizing from dual-frequency radar measurements, *J. Geophys. Res.*, **98**, 20,675–20,683.
- Matrosov, S. Y., B. W. Orr, R. A. Kropfli, and J. B. Snider (1994), Retrieval of vertical profiles of cirrus cloud microphysical parameters from Doppler radar and infrared radiometer measurements, *J. Appl. Meteorol.*, **33**, 617–626.
- Matrosov, S. Y., A. V. Korolev, and A. J. Heymsfield (2002), Profiling cloud mass and particle characteristic size from Doppler radar measurements, *J. Atmos. Oceanic Technol.*, **19**, 1003–1018.
- Matrosov, S. Y., S. D. Matthew, A. J. Heymsfield, and P. Zuidema (2003), Ice cloud optical thickness and extinction estimates from radar measurements, *J. Appl. Meteorol.*, **42**, 1584–1597.
- Mishchenko, M. I., and L. D. Travis (1998), Capabilities and limitations of a current Fortran implementation of the t-matrix method for randomly oriented, rotationally symmetric scatterers, *J. Quant. Spectrosc. Radiat. Transfer*, **60**, 309–324.
- Okamoto, H. (2002), Information content of the 95-GHz cloud radar signals: Theoretical assessment of effects of nonsphericity and error evaluation

- tion of the discrete dipole approximation, *J. Geophys. Res.*, 107(D22), 4628, doi:10.1029/2001JD001386.
- Sassen, K. (1987), Ice cloud content from radar reflectivity, *J. Clim. Appl. Meteorol.*, 26, 1050–1053.
- Sassen, K., Z. Wang, V. I. Khvorostyanov, G. L. Stephens, and A. Benedetti (2002), Cirrus cloud ice water content radar algorithm evaluation using an explicit cloud microphysical model, *J. Appl. Meteorol.*, 41, 620–628.
- Sekelsky, S. M., W. L. Ecklund, J. M. Firda, K. S. Gage, and R. E. McIntosh (1999), Particle size estimation in ice-phase cloud using multifrequency radar reflectivity measurements at 95, 33, and 2.8 GHz, *J. Appl. Meteorol.*, 38, 5–28.
- Twohy, C. H., A. J. Schanot, and W. A. Cooper (1997), Measurement of condensated water content in liquid and ice clouds using an airborne counterflow virtual impactor, *J. Atmos. Oceanic Technol.*, 14, 197–202.
- Vivekanandan, J., J. Turk, and V. N. Bringi (1991), Ice water path estimation and characterization using passive microwave radiometry, *J. Appl. Meteorol.*, 30, 1407–1421.
- Wang, J. R., G. Liu, J. D. Spinhirne, P. Racette, and W. D. Hart (2001), Observations and retrievals of cirrus cloud parameters using multichannel millimeter-wave radiometric measurements, *J. Geophys. Res.*, 106, 15,251–15,236.
- Wang, Z., and K. Sassen (2002), Cirrus cloud microphysical property retrieval using lidar and radar measurements, I: Algorithm description and comparison with in situ data, *J. Appl. Meteorol.*, 41, 218–229.
- Wang, Z., G. M. Heymsfield, L. Li, and A. J. Heymsfield (2004), Ice cloud microphysical property retrieval using airborne two-frequency radars, in *Microwave Remote Sensing of the Atmosphere and Environment IV*, edited by G. S. Jackson and S. Uratsuka, *Proc. SPIE*, 5654, 48–56.
- Weng, F., and N. C. Grody (2000), Retrieval of ice cloud parameters using a microwave imaging radiometer, *J. Atmos. Sci.*, 57, 1069–1083.
- Wielicki, B. A., R. D. Cess, M. D. King, D. A. Randall, and E. F. Harrison (1995), Mission to planet Earth: Role of clouds and radiation in climate, *Bull. Am. Meteorol. Soc.*, 76, 2125–2153.
- 
- A. J. Heymsfield, National Center for Atmospheric Research, 3450 Mitchell Lane, Boulder, CO 80307, USA.
- G. M. Heymsfield, NASA Goddard Space Flight Center, Code 613.1, Greenbelt, MD 20771, USA.
- L. Li, Goddard Earth Sciences and Technology Center, University of Maryland Baltimore County, Baltimore, MD 21228, USA.
- Z. Wang, Department of Atmospheric Science, University of Wyoming, 1000 E. University Avenue, Laramie, WY 82071, USA. (zwang@uwyo.edu)